Phase II Monitoring of Free-Form Surfaces: An Application to 3D Printing

Yangyang Zang[1] and Peihua Qiu[2]

[1]Department of Industrial Engineering, Tsinghua University

[2]Department of Biostatistics, University of Florida

The 3D printing technique becomes popular in recent years. Monitoring the quality of its products is thus important. In the literature, there is little existing research on this topic yet, partly because it is a challenging problem with complex data structures. In this paper, we propose a nonparametric control chart for Phase II monitoring of the top surfaces of 3D printing products. The top surfaces are focused in this paper because they are our major concern regarding the quality of 3D printing products in some applications. Such surfaces are often free-form surfaces. Our proposed method is based on local kernel estimation of free-form surfaces. Before Phase II monitoring, observed data from different products are first geometrically aligned, to account for possible movement between the products and a laser scanner during the data acquisition stage. Numerical studies show that the proposed method works well in practice.

Keywords: Image registration; Local smoothing; Nonparametric Regression; Process monitoring; Statistical process control; Surface estimation.

1 Introduction

The 3D printing is a process of synthesizing a 3D product formed by successive layers of material under computer control (Evans 2012). It has been used to create car parts, smartphone cases, fashion accessories, medical equipment, and artificial organs. Since the first functional 3D printer was created by Chuck Hull in 1984, this technology has come a long way ever since then. Then, a natural question arises: how can we monitor the quality of 3D printing products? This paper tries to make a contribution in answering this question.

Figure 1 shows a 3D printer, a 3D printing product, a laser scanner, and the observed data of a product's top surface. Before printing the product, users need to provide its designed shape to a computer system. Then, the printer prints the product under the control of the computer system. After a product is printed, the laser scanner generates the observed data of the product's shape surface, with the product fixed at a rotatable holder placed before the scanner. For the

product shown in Figure 1, we are mainly concerned about its curvy top surface, which is a free-form surface, because the quality of the product is reflected by the surface shape in this case. So, we only scan that surface. Its observed data are shown in the bottom-right panel of Figure 1. The data and the related devices shown in Figure 1 reveal several important features of the quality control problem for 3D printing products, which are briefly described below. i) The relative position between the laser scanner and the product can change from product to product, and the geometric deviation can involve directions, partly because the product holder is rotatable. Therefore, when monitoring the product's surface or shape, it is important to geometrically align the positions of the observed data of different products in advance. ii) The data volume is generally large. This requires computationally efficient statistical methods for analyzing the data and for monitoring the printing process. iii) The design points of the observed data may not be equally spaced and the shape of the product surface could be complicated. Therefore, the surface may not be described well by a parametric model, and our statistical methods should be able to accommodate unequally spaced design points. These features indicate that monitoring of 3D printing products is challenging.

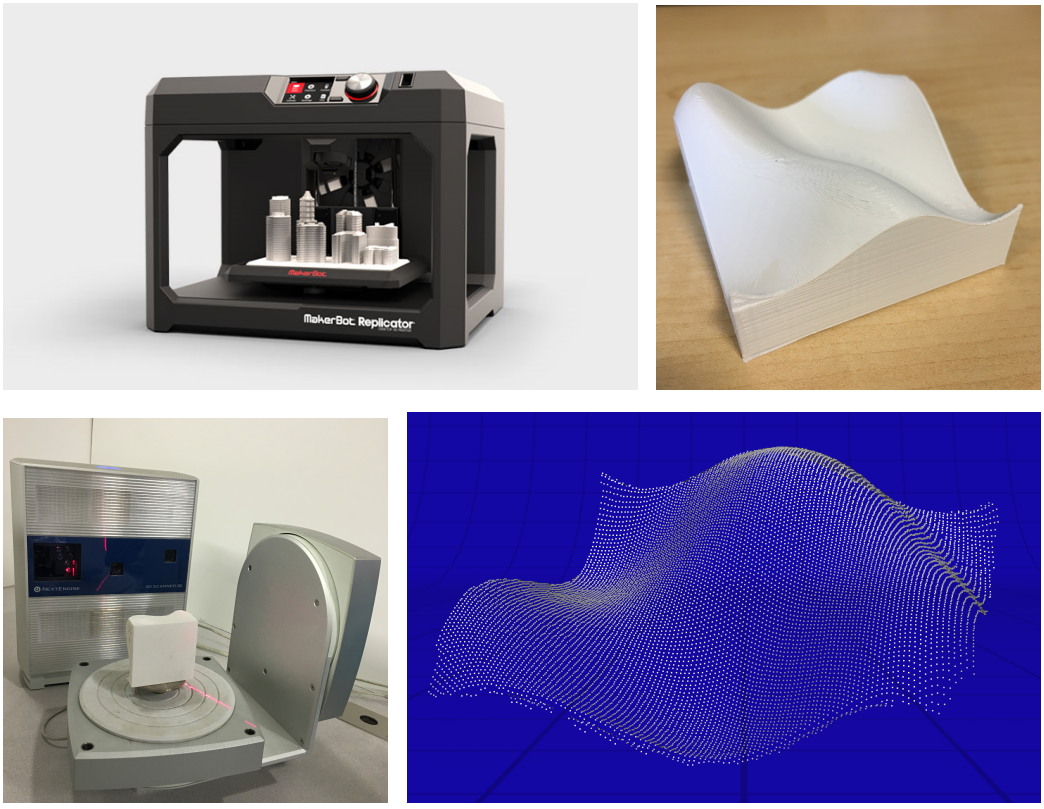

Figure 1: A 3D printer (top-left), a 3D printing product (top-right), a laser scanner (bottom-left), and the observed data of a product surface (bottom-right).

The process monitoring problem described above for 3D printing products is related to profile monitoring in the literature, where the observed top surface of a 3D printing product can be regarded as a profile. Early profile monitoring methods are based on linear or parametric modeling (e.g., Jin and Shi, 1999; Kang and Albin, 2000; Kim et al., 2003, Yeh et al. 2009). Recent methods are more flexible without requiring the parametric assumptions (e.g., Zou et al., 2008; Qiu et al., 2010). These methods are all univariate in the sense that the profile denotes the relationship between a response variable and a predictor. Multiple profile monitoring is under rapid development recently (e.g., Paynabar et al., 2013, 2016), which concerns the relationship between a predictor and multiple responses. Both the univariate and multiple profile monitoring problems discussed above are different from the current 3D printing monitoring problem in that the former focuses mainly on curve profiles while the latter is about surface profiles. In the literature, there are some recent discussions about surface profile monitoring. For instance, Wang et al. (2014) used a Gaussian-Kriging model to describe round wafer surface data and then proposed a Shewhart T^2 chart for surface monitoring. Colosimo et al. (2014) considered cylindrical surfaces and modeled them by a Gaussian process model that was also considered by some other papers, including Xia et al. (2008). These surface monitoring problems are substantially different from the current problem in the following sense. First, the Gaussian process models are used in these methods for describing the observed surfaces and their spatial data correlation. The Gaussian process models usually assume that observations at different locations are normally distributed and data correlation is spatially homogeneous (cf., Wang et al. 2014), which are difficult to verify in the current problem. Second, geometric alignment of different observed surfaces is not considered in Wang et al. (2014). In Colosimo et al. (2014), geometric alignment of different surfaces is based on the assumed cylindrical surface structure. It is achieved by first aligning the centers of different surfaces and then maximizing the cross-correlation between roundness profiles of the surfaces. This registration approach cannot be used in the current problem with free-form surfaces.

Recently, Zang and Qiu (2017) discussed Phase I monitoring of 3D printing products, where the focus is on detecting outliers among a given set of 3D printing products using a Shewhart chart. In this paper, we propose a nonparametric CUSUM chart for Phase II online monitoring of 3D printing products. Our method focuses mainly on monitoring the top surfaces of the products since they are often our concern regarding the 3D printing quality in many applications. Our method will be described in detail in Section 2. Its performance is evaluated by simulation examples in

Section 3. A real-data example is discussed in Section 4. Some remarks conclude the article in Section 5.

2 Phase II Monitoring of Free-Form Surfaces in 3D Printing

Our proposed Phase II online monitoring procedure has three major components. i) *Surface registration:* all observed top surfaces of 3D printing products are geometrically aligned. ii) *Nonparametric surface estimation:* The IC top surface and other IC quantities are estimated from an IC dataset, using a nonparametric local kernel smoothing procedure. iii) *Online process monitoring:* a Phase II nonparametric CUSUM chart is then constructed for online monitoring of 3D printing products. These components are described in detail below.

2.1 Surface estimation and registration

From the introduction of data acquisition in Section 1 (cf., Figure 1), we can see that the relative positions between the laser scanner and individual 3D printing products could change from product to product. Therefore, different observed surfaces should be geometrically aligned before surface monitoring. This is similar to the image registration problem in the image processing literature if the height of a surface at a given point is regarded as the image intensity (cf., Bhagalia et al., 2009; Pan et al., 2009; Xing and Qiu, 2011). Image registration is mainly for estimating a geometric transformation to geometrically match one image to another. Both parametric (Denton et al., 1999) and nonparametric (Qiu and Xing, 2013) transformations have been considered in the literature. In the current surface registration problem, the transformation for describing the geometric movement is rigid-body in the sense that the Euclidean distance between any two points on a surface will not change after the transformation, which can be described by the following expression:

$$(x^{(1)}, y^{(1)}, z^{(1)})' = \mathbf{R}(x^{(2)}, y^{(2)}, z^{(2)})' + \mathbf{T}, \tag{1}$$

where $(x^{(1)}, y^{(1)}, z^{(1)})'$ and $(x^{(2)}, y^{(2)}, z^{(2)})'$ are the corresponding points on the two images, $\mathbf{T} = (T_x, T_y, T_z)'$ describes location shifts in the x, y, and z directions, $\mathbf{R}$ is a rotation matrix with the

expression

$$\mathbf{R} = \begin{bmatrix} 1 & 0 & 0 \\ 0 & \cos\alpha & \sin\alpha \\ 0 & -\sin\alpha & \cos\alpha \end{bmatrix} \begin{bmatrix} \cos\beta & 0 & -\sin\beta \\ 0 & 1 & 0 \\ \sin\beta & 0 & \cos\beta \end{bmatrix} \begin{bmatrix} \cos\theta & \sin\theta & 0 \\ -\sin\theta & \cos\theta & 0 \\ 0 & 0 & 1 \end{bmatrix}, \tag{2}$$

and $\mathbf{A} = (\alpha, \beta, \theta)'$ are rotating angles along the x, y, and z axes. To register the two surfaces, we need to estimate the parameters $\mathbf{T}$ and $\mathbf{A}$ in the above transformation from the two observed surfaces, which is briefly discussed below.

Assume that observations of two observed surfaces follow the model

$$z_{ij} = g_i(x_{ij}, y_{ij}) + \varepsilon_{ij}, \qquad \text{for } j = 1, 2, \ldots, N_i, \;\; i = 1, 2, \tag{3}$$

where $g_i(x, y)$ is the true regression function for describing the ith surface, $\{(x_{ij}, y_{ij})\}$ are design points in the design space Ω, and ε_{ij}'s are random errors with mean 0 and variance σ^2. In the statistical literature (Qiu 2005, Chapter 2), there are two types of nonparametric smoothing methods for estimating regression surfaces: the global smoothing approaches (e.g., smoothing splines) and the local smoothing approaches (e.g., kernel smoothing). By a global smoothing approach, all available observations are used in estimating a regression surface at a specific location. So, its computation is extensive. As a comparison, to estimate the regression surface at a specific location by a local smoothing approach, only those observations located in a neighborhood of the given location are used. Thus, its computation is relatively simple and fast. For this reason and the facts that the number of observations for each surface in the current problem is often large and the surface shape could be complex (cf., the related discussion in Section 1), we choose to estimate $g_i(x, y)$ using the following Nadaraya-Watson (NW) kernel smoothing procedure (Qiu 2005, Section 2.3): for $i = 1, 2$,

$$\widehat{g}_i(x, y) = \sum_{j=1}^{N_i} z_{ij} K\left(\frac{x_{ij} - x}{h}, \frac{y_{ij} - y}{h}\right) \Bigg/ \sum_{j=1}^{N_i} K\left(\frac{x_{ij} - x}{h}, \frac{y_{ij} - y}{h}\right), \tag{4}$$

where K is a two-dimensional, circularly symmetric kernel function with a unit circular support, and $h > 0$ is a bandwidth. Because the NW estimator $\widehat{g}_i(x, y)$ weightedly averages observations in the local circular neighborhood of (x, y) with radius determined by h for estimating $g_i(x, y)$ and observations outside the neighborhood is not involved, its computation is fast. Then, $\mathbf{T}$ and $\mathbf{A}$ can be estimated by

$$\min_{\mathbf{T},\mathbf{A}} \sum_{i'=1}^{\widetilde{n}_x} \sum_{j'=1}^{\widetilde{n}_y} \left| \widehat{g}_2(\widetilde{x}^*_{i'j'}, \widetilde{y}^*_{i'j'}) - \widehat{g}_1(\widetilde{x}_{i'j'}, \widetilde{y}_{i'j'}) \right|, \tag{5}$$

where $\{(\widetilde{x}_{i'j'}, \widetilde{y}_{i'j'}), i' = 1, 2, \ldots, \widetilde{n}_x, j' = 1, 2, \ldots, \widetilde{n}_y\}$ is an equally spaced grid that covers the entire design space Ω, and $\widetilde{x}^*_{i'j'}$ and $\widetilde{y}^*_{i'j'}$ are the first two components of $\mathbf{R}(\widetilde{x}_{i'j'}, \widetilde{y}_{i'j'}, \widehat{g}_2(\widetilde{x}_{i'j'}, \widetilde{y}_{i'j'}))' + \mathbf{T}$ that is defined in (1).

There are a total of 6 parameters to estimate in (5), which is computationally intensive. To simplify the computation, we adopt the suggestion by Audette et al. (2000) that the three translation parameters can be determined first by aligning the centers of the two related surfaces. Namely, they can be estimated by

$$\widehat{T}_x = \frac{1}{N_1}\sum_{j=1}^{N_1} x_{1j} - \frac{1}{N_2}\sum_{j=1}^{N_2} x_{2j}, \quad \widehat{T}_y = \frac{1}{N_1}\sum_{j=1}^{N_1} y_{1j} - \frac{1}{N_2}\sum_{j=1}^{N_2} y_{2j}, \quad \widehat{T}_z = \frac{1}{N_1}\sum_{j=1}^{N_1} z_{1j} - \frac{1}{N_2}\sum_{j=1}^{N_2} z_{2j}. \quad (6)$$

Then, we can replace $\mathbf{T}$ by $\widehat{\mathbf{T}} = (\widehat{T}_x, \widehat{T}_y, \widehat{T}_z)$ in (5) and search for the values of the estimates of the three rotation parameters by the following iterative searching algorithm.

(i) Set the initial values for $\mathbf{A} = (\alpha, \beta, \theta)$ to be $\mathbf{A}^{(0)} = (0, 0, 0)$.

(ii) In the ℓth iteration, for $\ell \geq 1$, evaluate the objective function

$$\sum_{i'=1}^{\widetilde{n}_x}\sum_{j'=1}^{\widetilde{n}_y} \left|\widehat{g}_2(\widetilde{x}^*_{i'j'}, \widetilde{y}^*_{i'j'}) - \widehat{g}_1(\widetilde{x}_{i'j'}, \widetilde{y}_{i'j'})\right|$$

at all $3^3 = 27$ possible values of $\mathbf{A}$ with each component being the value obtained in the previous iteration or that value $\pm d_\ell$, where d_ℓ is a constant depending on ℓ. The minimizer is denoted as $\mathbf{A}^{(\ell)}$.

(iii) The procedure stops if $\max(|\alpha^{(\ell)} - \alpha^{(\ell-1)}|, |\beta^{(\ell)} - \beta^{(\ell-1)}|, |\theta^{(\ell)} - \theta^{(\ell-1)}|) < \epsilon$, where $\epsilon > 0$ is a given small number.

The resulting estimates are denoted as $\widehat{\mathbf{A}} = (\widehat{\alpha}, \widehat{\beta}, \widehat{\theta})$.

2.2 Phase II online monitoring

For Phase II process monitoring, the true top surface of an IC 3D printing product, denoted as $g^{(0)}(x, y)$, should be known. In reality, it is usually unknown, and needs to be estimated from an IC data. Assume that there are m observed surfaces in an IC data. After surface registration with an observed surface in the IC data, let the surface estimates from the m observed surfaces (cf.,

(4)) be $\{\widetilde{g}_i^*(x,y), i=1,2,\ldots,m\}$. Then, we can define $\widehat{g}^{(0)}(x,y)=\frac{1}{m}\sum_{i=1}^{m}\widetilde{g}_i^*(x,y)$. Theoretically speaking, any surface in the IC data can be chosen as the baseline surface with which other surfaces are registered for computing $\widehat{g}^{(0)}(x,y)$. In practice, the results would not change much if different baseline surfaces are used. So, for convenience, the first surface can be used as the baseline surface.

Assume that the ith observed surface in a Phase II 3D printing process follows the model

$$z_{ij}=g_i(x_{ij},y_{ij})+\varepsilon_{ij}, \qquad \text{for } j=1,2,\ldots,N_i, \;\; i=1,2,\ldots, \tag{7}$$

where the related quantities are defined similarly to those in model (3). So, if the process is IC at the ith time point and no surface registration is needed, then $g_i(x,y)=g^{(0)}(x,y)$. However, surface registration is necessary in monitoring the 3D printing process, as discussed in Section 1. To this end, we estimate each Phase II surface by the NW kernel estimation procedure (4), and then register it with $\widehat{g}^{(0)}(x,y)$. After these surface pre-processing steps, the geometrically aligned and estimated Phase II surfaces are denoted as $\{\widehat{g}_i^*(x,y), i=1,2,\ldots\}$, where $\widehat{g}_i^*(x,y)=\widehat{g}_i(x^*,y^*)$, x^* and y^* are the first two components of $\widehat{\mathbf{R}}_i(x,y,\widehat{g}_2(x,y)'+\widehat{\mathbf{T}}_i$ (cf., (1)), $\widehat{\mathbf{R}}_i$ and $\widehat{\mathbf{T}}_i$ are the estimated rotation matrix and location shifts in the rigid-body surface registration procedure discussed in the previous part when matching the ith estimated surface with $\widehat{g}^{(0)}(x,y)$.

Let $\{(\widetilde{x}_{i'j'},\widetilde{y}_{i'j'}), i'=1,2,\ldots,\widetilde{n}_x, j'=1,2,\ldots,\widetilde{n}_y\}$ be an equally spaced grid that covers the entire design space Ω, as in (5). Then, the overall difference between the ith aligned estimated Phase II surface and $\widehat{g}^{(0)}(x,y)$ can be measured by

$$\Lambda_{ART,i}=\frac{1}{\widetilde{n}_x\widetilde{n}_y}\sum_{i'=1}^{\widetilde{n}_x}\sum_{j'=1}^{\widetilde{n}_y}\left|\widehat{g}_i^*(x_{i'j'},y_{i'j'})-g^{(0)}(x_{i'j'},y_{i'j'})\right|, \tag{8}$$

where the subscripts "A", "R" and "T" denote the absolute value norm used in (8), the rotation and translation considered in the surface registration, respectively. Thus, a natural CUSUM charting statistic can be defined by

$$Q_{ART,i}^{+}=\max\Big(0,Q_{ART,i-1}^{+}+\frac{\Lambda_{ART,i}-\mathrm{E}_0(\Lambda_{ART,i})}{\sqrt{\mathrm{Var}_0(\Lambda_{ART,i})}}-k\Big), \qquad i=1,2,\ldots, \tag{9}$$

where $Q_{ART,0}^{+}=0$, $\mathrm{E}_0(\Lambda_{ART,i})$ and $\mathrm{Var}_0(\Lambda_{ART,i})$ are the IC mean and variance of $\Lambda_{ART,i}$, respectively, and k is the allowance constant. The chart gives a signal of surface shift when

$$Q_{ART,i}^{+}>c_{ART}, \tag{10}$$

where $c_{ART}>0$ is a control limit.

To use the CUSUM chart (9)-(10), we need to determine the quantities $\mathrm{E}_0(\Lambda_{ART,i})$, $\mathrm{Var}_0(\Lambda_{ART,i})$, k and c_{ART}, which is discussed below. Obviously, when all products are IC, the charting statistic Q^+_{ART} in (9) does not depend on $g^{(0)}(x,y)$ and $g_i(x,y)$ much, for $i=1,2,\ldots$, because $g^*_i(x,y)=g^{(0)}(x,y)$ in such cases and Q^+_{ART} is based mainly on $g^*_i(x,y)-g^{(0)}(x,y)$, where $g^*_i(x,y)$ denotes the ith aligned surface. Based on this observation, the quantities $\mathrm{E}_0(\Lambda_{ART,i})$ and $\mathrm{Var}_0(\Lambda_{ART,i})$ can be approximated using the IC data as follows. For each registered and estimated surface $\widetilde{g}^*_i(x,y)$ in the IC data (cf., the discussion at the beginning of this part), compute

$$\widetilde{\Lambda}_{ART,i}=\frac{1}{\widetilde{n}_x\widetilde{n}_y}\sum_{i'=1}^{\widetilde{n}_x}\sum_{j'=1}^{\widetilde{n}_y}\left|\widetilde{g}^*_i(x_{i'j'},y_{i'j'})-\widehat{g}^{(0)}(x_{i'j'},y_{i'j'})\right|, \qquad \text{for } i=1,2,\ldots,m.$$

Then, $\mathrm{E}_0(\Lambda_{ART,i})$ and $\mathrm{Var}_0(\Lambda_{ART,i})$ can be approximated by the sample mean and variance of $\{\widetilde{\Lambda}_{ART,i}, i=1,2,\ldots,m\}$. Regarding k and c_{ART}, usually k is chosen beforehand, and then c_{ART} is chosen such that the CUSUM chart (9)-(10) can reach the pre-specified ARL_0 value. Commonly used k values include $0.1, 0.25, 0.5, 0.75$ and 1. Once k is chosen, c_{ART} can be determined by the following block bootstrap procedure. First, select one observed surface from the IC data. Without loss of generality, let us assume that it is the $\widetilde{i}$th surface. Then, define the set of IC residuals of the $\widetilde{i}$th surface by

$$\mathcal{D}_{\widetilde{i}}=\{\widetilde{g}^*_{\widetilde{i}}(x_{i'j'},y_{i'j'})-\widehat{g}^{(0)}(x_{i'j'},y_{i'j'}),\ \text{ for } i'=1,2,\ldots,\widetilde{n}_x, j'=1,2,\ldots,\widetilde{n}_y\}.$$

Second, select $\widetilde{n}_x\widetilde{n}_y$ elements with replacement from $\mathcal{D}_{\widetilde{i}}$ as the quantities of the ith surface of a Phase II process used in (8), and calculate the mean of their absolute values as $\Lambda_{ART,i}$. Then, the CUSUM charting statistic value $Q^+_{ART,i}$ can be calculated by (9). For a given value of c_{ART}, continue the above process until a signal is given according to (10). Then, a run length can be determined. Third, repeat the above two steps for B times and the average of the B run lengths can be calculated as an approximation to the actual ARL_0 value. If this value is smaller than the assumed ARL_0 value, then increase the specified c_{ART} value. Otherwise, decrease the specified c_{ART} value. The above three steps are executed recursively until the assumed ARL_0 value is reached within certain precision. In this process for searching for the value of c_{ART}, the bisection searching algorithm or other numerically efficient algorithms can be applied. See a related discussion in Section 4.2 in Qiu (2014).

3 Simulation Study

In this section, we present some numerical results regarding the performance of the proposed method. Besides the chart $Q^+_{ART,i}$ defined in (9)-(10), we also consider the following three alternative methods: the chart with L_2 norm in (5) and (8) (i.e., the absolute value is replaced by the square) and with both rotation and translation in surface registration, denoted as $Q^+_{SRT,i}$, the chart with L_1 norm in (5) and (8) and with translation only in surface registration (i.e. rotation is ignored), denoted as $Q^+_{AT,i}$, and the chart with L_1 norm in (5) and (8) and without surface registration, denoted as $Q^+_{A,i}$. In all these methods, we use the truncated Gaussian kernel function $K(u,v) = \exp[-(u^2+v^2)/2]I(u^2+v^2 \le 20)$ in the NW kernel estimation procedure (4) and the bandwidth is first chosen to be $h = 0.1$. The above charts are considered here because (i) $Q^+_{ART,i}$ is recommended based on our numerical results, and (ii) $Q^+_{AT,i}$ and $Q^+_{A,i}$ are included for demonstrating the consequence when rotation and translation are present in the geometric transformation (1) but they are ignored in surface registration.

In the simulation, we consider the design space $\Omega = [-10,10] \times [-10,10]$, the IC surface

$$g^{(0)}(x,y) = xy \exp\left\{ -\left(\frac{1.5x}{10}\right)^2 - \left(\frac{3y}{10}\right)^2 \right\} + 5,$$

and the following three OC surfaces

$$\begin{aligned}
g^{(1)}(x,y) &= g^{(0)}(x,y) + r_1 xy \exp\left\{ -\left(\frac{1.5x}{10}\right)^2 - \left(\frac{3y}{10}\right)^2 \right\} I(x>0, y>0), \\
g^{(2)}(x,y) &= g^{(0)}(x,y) + r_2 xy \exp\left\{ -\left(\frac{1.5x}{10}\right)^2 - \left(\frac{3y}{10}\right)^2 \right\}, \\
g^{(3)}(x,y) &= g^{(0)}(x,y) + \eta(x^2+y^2)/10^2,
\end{aligned}$$

where $r_1 = 0.01, 0.03, \ldots, 0.21$, $r_2 = 0.005, 0.010, \ldots, 0.080$, and $\eta = 0.01, 0.03, \ldots, 0.29$. The OC surface $g^{(1)}(x,y)$ is different from the IC surface $g^{(0)}(x,y)$ in the upper-right quadrant only, $g^{(2)}(x,y)$ is different from $g^{(0)}(x,y)$ in the entire design space with the difference small in the central and border regions of the design space, and $g^{(3)}(x,y)$ is also different from $g^{(0)}(x,y)$ in the entire design space with the difference large in the border regions of the design space.

The observed surfaces are generated from model (7) with the random errors ε_{ij} generated i.i.d. from the $N(0, 0.15^2)$ distribution. The observation locations $\{(x_{ij}, y_{ij})\}$ for the ith surface are generated in two steps as follows. First, an equally spaced grid is generated in Ω with the

distance between two consecutive horizontal or vertical lines being 0.1. Each grid point is then moved horizontally by s_h and vertically by s_v, where s_h and s_v are two independent random numbers generated from the $N(0, 0.02^2)$ distribution. The set of the resulting disturbed grid points is called *a disturbed grid*. Second, for the ith observed surface, generate an integer number N_i from the $U(15000, 16000)$ distribution as the number of observations of that surface. Then, the observation locations $\{(x_{ij}, y_{ij}), j = 1, 2, \ldots, N_i\}$ are obtained by randomly selecting N_i points without replacement from the disturbed grid.

In the IC dataset, all observed surfaces are first rotated α, β and θ degrees in the x, y, and z axes, respectively, where (α, β, θ) are independent random numbers generated from the $U[-3, 3]$ distribution, and then moved respectively by T_x, T_y and T_z along the three axes, where (T_x, T_y, T_z) are independent random numbers generated from the $U[-1, 1]$ distribution. All surfaces observed in the Phase II process are also taken such geometric transformations after they are generated in the way described in the previous paragraph from an OC model.

When the nominal ARL_0 value is set at 20, and k is chosen to be 0.1 or 0.5, the control limit values of the four CUSUM charts considered in this section are computed based on 5,000 repeated simulations. The results are presented in Table 1. Then, for the three OC surfaces, the computed ARL_1 values based on 2000 replicated simulations, when k equals 0.1 or 0.5 and when the parameters in the three OC surfaces take various different values, are presented in Tables 2-4. Numbers in parentheses are standard errors of the ARL_1 values. From the tables, we can have the following conclusions. (i) For the first OC surface that shifts from $g^{(0)}(x, y)$ in the upper-right quadrant only, both $Q^+_{SRT,i}$ and $Q^+_{ART,i}$ performs well, $Q^+_{AT,i}$ performs much worse than the first two charts, and $Q^+_{A,i}$ is the worst. (ii) For the second OC surface that shifts from $g^{(0)}(x, y)$ in the entire design space with their difference small in the central and border regions, the conclusions are similar to those in (i), except that $Q^+_{ART,i}$ seems to perform better than $Q^+_{SRT,i}$ in this case. (iii) For the third OC surface that shifts from $g^{(0)}(x, y)$ in the entire design space with their difference large in the border regions, the advantage of $Q^+_{ART,i}$ over $Q^+_{SRT,i}$ is more obvious, and other conclusions are similar to those in (i). Therefore, based on this simulation study, we can see that surface registration is a necessary pre-processing for surface monitoring in cases when geometric misalignment is a real issue. Also, between $Q^+_{SRT,i}$ and $Q^+_{ART,i}$, it seems that $Q^+_{ART,i}$ has some advantage. From Tables 2 and 4, it can be noticed that the chart $Q^+_{A,i}$ is biased in certain cases when its ARL_1 values are larger than the nominal ARL_0 value. That is because this chart does not consider surface

registration in advance, and consequently its charting statistic has larger values in the case when no surface shift is present, compared to certain cases when there are surface shifts (because of the surface misalignment between the observed surfaces and the IC surface $g^{(0)}(x, y)$).

Table 1: Control limits of the four CUSUM charts when $ARL_0 = 20$ and k is chosen to be 0.1 or 0.5.

$Q^+_{SRT,i}$		$Q^+_{ART,i}$		$Q^+_{AT,i}$		$Q^+_{A,i}$	
$k = 0.1$	$k = 0.5$	$k = 0.1$	$k = 0.5$	$k = 0.1$	$k = 0.5$	$k = 0.1$	$k = 0.5$
2.62	1.49	2.50	1.44	5.75	2.28	2.11	1.18

Table 2: ARL_1 values of the Phase II CUSUM charts when $ARL_0 = 20$, $k = 0.1$ or 0.5, the OC surface is $g^{(1)}(x, y)$, and the shift parameter r_1 takes various different values. Numbers in parentheses are standard errors.

r_1	$Q^+_{SRT,i}$		$Q^+_{ART,i}$		$Q^+_{AT,i}$		$Q^+_{A,i}$	
	$k = 0.1$	$k = 0.5$	$k = 0.1$	$k = 0.5$	$k = 0.1$	$k = 0.5$	$k = 0.1$	$k = 0.5$
0	20.43(0.40)	20.08(0.41)	19.55(0.38)	19.82(0.41)	20.01(0.26)	20.01(0.39)	19.92(0.39)	20.18(0.44)
0.01	17.70(0.35)	18.61(0.39)	18.12(0.35)	18.43(0.38)	20.16(0.27)	19.52(0.39)	19.89(0.41)	20.35(0.44)
0.03	11.11(0.20)	13.07(0.28)	10.67(0.19)	12.39(0.25)	18.12(0.25)	17.59(0.34)	20.11(0.41)	21.95(0.46)
0.05	5.95(0.08)	6.53(0.12)	5.30(0.07)	6.28(0.11)	16.57(0.21)	15.24(0.28)	19.84(0.40)	21.49(0.45)
0.07	3.45(0.04)	3.39(0.05)	3.29(0.03)	3.10(0.05)	14.47(0.16)	12.87(0.24)	19.59(0.36)	23.08(0.48)
0.09	2.24(0.02)	1.91(0.02)	2.19(0.02)	1.88(0.02)	12.88(0.15)	10.85(0.19)	20.49(0.41)	23.18(0.49)
0.11	1.62(0.01)	1.30(0.01)	1.69(0.01)	1.37(0.01)	11.45(0.12)	9.43(0.16)	19.75(0.38)	24.91(0.53)
0.13	1.21(0.01)	1.06(0.01)	1.28(0.01)	1.10(0.01)	9.97(0.10)	7.87(0.13)	19.75(0.39)	23.51(0.49)
0.15	1.03(0.00)	1.00(0.00)	1.08(0.01)	1.01(0.00)	9.01(0.09)	6.74(0.11)	19.81(0.39)	24.11(0.50)
0.17	1.00(0.00)	1.00(0.00)	1.01(0.00)	1.00(0.00)	7.99(0.07)	5.86(0.09)	18.93(0.36)	24.78(0.53)
0.19	1.00(0.00)	1.00(0.00)	1.00(0.00)	1.00(0.00)	7.22(0.06)	5.09(0.07)	19.64(0.38)	23.21(0.49)
0.21	1.00(0.00)	1.00(0.00)	1.00(0.00)	1.00(0.00)	6.63(0.06)	4.53(0.06)	18.70(0.36)	24.34(0.52)

Table 3: ARL_1 values of the Phase II CUSUM charts when $ARL_0 = 20$, $k = 0.1$ or 0.5, the OC surface is $g^{(2)}(x, y)$, and the shift parameter r_2 takes various different values. Numbers in parentheses are standard errors.

r_2	$Q^+_{SRT,i}$		$Q^+_{ART,i}$		$Q^+_{AT,i}$		$Q^+_{A,i}$	
	$k = 0.1$	$k = 0.5$	$k = 0.1$	$k = 0.5$	$k = 0.1$	$k = 0.5$	$k = 0.1$	$k = 0.5$
0	20.43(0.40)	20.08(0.41)	19.55(0.38)	19.82(0.41)	20.01(0.26)	20.01(0.39)	19.92(0.39)	20.18(0.44)
0.005	17.91(0.34)	18.19(0.38)	16.31(0.30)	17.17(0.35)	19.80(0.27)	20.04(0.41)	19.78(0.39)	19.95(0.42)
0.010	12.94(0.24)	14.67(0.31)	12.08(0.22)	13.56(0.28)	18.75(0.25)	17.88(0.33)	18.91(0.37)	19.14(0.40)
0.015	9.36(0.15)	10.70(0.21)	8.08(0.13)	9.03(0.18)	18.36(0.23)	18.00(0.33)	19.54(0.39)	20.00(0.42)
0.020	6.46(0.09)	7.34(0.14)	5.29(0.07)	5.78(0.10)	17.32(0.22)	17.06(0.32)	18.24(0.34)	18.06(0.37)
0.025	4.55(0.05)	4.86(0.08)	3.66(0.04)	3.73(0.06)	16.35(0.20)	15.70(0.31)	18.74(0.36)	19.32(0.41)
0.030	3.24(0.03)	3.18(0.05)	2.66(0.02)	2.51(0.03)	15.24(0.17)	14.25(0.26)	18.10(0.36)	18.54(0.38)
0.035	2.52(0.02)	2.26(0.03)	2.13(0.02)	1.82(0.02)	14.29(0.16)	12.92(0.24)	17.35(0.34)	17.88(0.39)
0.040	2.06(0.02)	1.71(0.02)	1.72(0.01)	1.42(0.01)	13.63(0.15)	12.28(0.22)	17.53(0.35)	18.40(0.37)
0.045	1.68(0.01)	1.36(0.01)	1.44(0.01)	1.17(0.01)	12.29(0.13)	10.94(0.19)	17.61(0.35)	17.87(0.38)
0.050	1.42(0.01)	1.16(0.01)	1.21(0.01)	1.06(0.01)	11.38(0.11)	9.90(0.17)	16.17(0.30)	17.75(0.38)
0.055	1.19(0.01)	1.05(0.00)	1.06(0.01)	1.01(0.00)	10.67(0.10)	9.10(0.15)	16.67(0.33)	17.18(0.35)
0.060	1.07(0.01)	1.01(0.00)	1.01(0.00)	1.00(0.00)	9.75(0.09)	8.38(0.13)	15.99(0.31)	16.68(0.35)
0.065	1.02(0.00)	1.00(0.00)	1.00(0.00)	1.00(0.00)	9.20(0.08)	7.21(0.11)	15.73(0.32)	16.20(0.33)
0.070	1.00(0.00)	1.00(0.00)	1.00(0.00)	1.00(0.00)	8.41(0.07)	6.59(0.09)	15.10(0.29)	16.19(0.34)
0.075	1.00(0.00)	1.00(0.00)	1.00(0.00)	1.00(0.00)	7.82(0.06)	5.72(0.08)	15.33(0.29)	15.79(0.33)
0.080	1.00(0.00)	1.00(0.00)	1.00(0.00)	1.00(0.00)	7.36(0.06)	5.46(0.07)	14.97(0.27)	16.27(0.34)

Table 4: ARL_1 values of the Phase II CUSUM charts when $ARL_0 = 20$, $k = 0.1$ or 0.5, the OC surface is $g^{(3)}(x, y)$, and the shift parameter η takes various different values. Numbers in parentheses are standard errors.

η	$Q^+_{SRT,i}$		$Q^+_{ART,i}$		$Q^+_{AT,i}$		$Q^+_{A,i}$	
	$k = 0.1$	$k = 0.5$	$k = 0.1$	$k = 0.5$	$k = 0.1$	$k = 0.5$	$k = 0.1$	$k = 0.5$
0	20.43(0.40)	20.08(0.41)	19.55(0.38)	19.82(0.41)	20.01(0.26)	20.01(0.39)	19.92(0.39)	20.18(0.44)
0.01	20.10(0.40)	19.73(0.41)	19.46(0.38)	20.28(0.43)	19.49(0.25)	20.09(0.38)	21.34(0.42)	21.11(0.44)
0.03	17.49(0.34)	17.81(0.37)	18.43(0.34)	17.99(0.39)	19.57(0.26)	19.22(0.38)	21.26(0.42)	23.10(0.52)
0.05	14.88(0.27)	15.52(0.33)	14.69(0.28)	15.33(0.32)	19.71(0.26)	19.02(0.37)	21.63(0.44)	24.63(0.53)
0.07	11.73(0.21)	13.25(0.28)	11.05(0.19)	12.79(0.27)	18.63(0.24)	18.68(0.36)	23.64(0.47)	27.34(0.57)
0.09	8.71(0.14)	10.30(0.20)	8.19(0.13)	9.68(0.20)	18.55(0.24)	17.74(0.34)	23.50(0.48)	29.47(0.62)
0.11	6.40(0.10)	7.66(0.14)	5.91(0.08)	6.89(0.13)	17.35(0.21)	17.65(0.36)	25.04(0.51)	30.49(0.64)
0.13	4.90(0.06)	5.27(0.09)	4.36(0.05)	4.43(0.07)	17.36(0.21)	16.19(0.30)	25.63(0.51)	34.05(0.71)
0.15	3.78(0.04)	3.88(0.06)	3.27(0.03)	3.25(0.05)	16.19(0.19)	15.63(0.29)	27.25(0.55)	36.42(0.74)
0.17	3.07(0.03)	2.82(0.04)	2.66(0.03)	2.48(0.03)	15.46(0.19)	13.95(0.25)	28.88(0.56)	39.93(0.82)
0.19	2.49(0.02)	2.26(0.03)	2.17(0.02)	1.90(0.02)	14.64(0.17)	13.19(0.24)	29.75(0.59)	42.85(0.86)
0.21	2.10(0.02)	1.80(0.02)	1.83(0.01)	1.56(0.02)	13.76(0.15)	12.88(0.23)	31.07(0.62)	45.30(0.90)
0.23	1.82(0.01)	1.53(0.02)	1.57(0.01)	1.28(0.01)	13.24(0.14)	11.90(0.21)	32.03(0.66)	46.65(0.93)
0.25	1.59(0.01)	1.30(0.01)	1.38(0.01)	1.16(0.01)	12.25(0.12)	10.70(0.18)	33.20(0.67)	52.00(0.98)
0.27	1.39(0.01)	1.16(0.01)	1.20(0.01)	1.06(0.01)	11.41(0.12)	10.13(0.18)	32.97(0.66)	53.19(0.99)
0.29	1.23(0.01)	1.06(0.01)	1.09(0.01)	1.01(0.00)	10.77(0.10)	9.04(0.15)	35.18(0.68)	54.95(1.03)

In the above examples, the bandwidth h used in surface estimation (cf., (4)) is fixed at 0.1. As pointed out in Section 2.4 of Qiu (2005), the bandwidth determines how many observations around a given point (x, y) when we estimate a surface at (x, y). If it is chosen larger, then more observations will be used and the resulting surface estimate would be smoother. However, more curved parts of the true surface would be smoothed out as well. So, there is a trade-off between noise removal ability and estimation bias when we consider different values of h in surface estimation. In the setup of Table 2, we change the h value from 0.05 to 0.3 with a step of 0.05, the calculated ARL_1 values of the charts $Q^+_{ART,i}$ and $Q^+_{SRT,i}$ when $k = 0.1$ and $r_1 = 0.05$ are shown in Figure 2. From the plot, it can be seen that the ARL_1 values decrease when h increases in this example, and the results stabilize when $h > 0.2$. In the function estimation literature, it has been well discussed that properties of the estimated function by the kernel smoothing method (e.g., (4)) depend on many different factors, including the curvature of the true function, the noise level, the sample size, and the bandwidth (e.g., Qiu 2005).

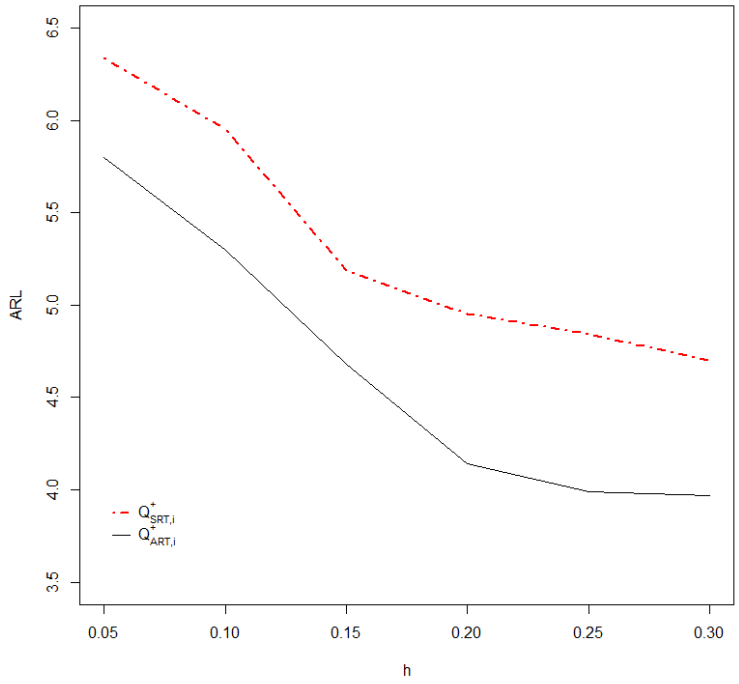

Figure 2: Calculated ARL_1 values of the charts $Q^+_{ART,i}$ and $Q^+_{SRT,i}$ when $ARL_0 = 20$, $k = 0.1$ and $r_1 = 0.05$ in the setup of Table 2.

In the examples discussed above, the noise level is fixed at $\sigma = 0.15$. When the noise level increases, performance of the related charts would get worse. To confirm this, we considered cases

when $\sigma = 0.5$ or 1.0, in the setup of Table 2 with $k = 0.1$ and $r_1 = 0.05$. The ARL_1 values of the chart $Q^+_{ART,i}$ are 13.70 and 17.31, respectively, when $\sigma = 0.5$ and 1.0, both of which are much larger than the corresponding value 5.30 that are presented in Table 2. In the above examples, the unequally-spaced design points are generated by using the disturbers s_h and s_v in the horizontal and vertical directions, respectively. If the variability of these two disturbers is larger, then the design points would be more unequally-spaced. Next, we study the impact of the variability of s_h and s_v on the performance of the chart $Q^+_{ART,i}$. For simplicity, let the standard deviations of s_h and s_v to be the same as σ_s. The disturbed grid is still generated in the same way as that in the example of Table 2. When σ_s changes from 0.01, 0.02, 0.05 to 0.1, the calculated ARL_1 values of the chart $Q^+_{ART,i}$ are 5.88, 5.84, 5.78 and 5.63, respectively, when $k = 0.1$ and $r_1 = 0.05$ in the setup of Table 2. We can see that the variability in the design points actually benefits the chart $Q^+_{ART,i}$ in the cases considered, although the impact is relatively small.

Next, using the example of Table 2, we compare the proposed control chart $Q^+_{ART,i}$ with the Gaussian-Kriging (GK) method suggested by Wang et al. (2014) and the Gaussian process (GP) method discussed in Colosimo et al. (2014). The original GK method provides a Shewhart chart that is based on a Hotelling's T^2 statistic, which is denoted as GK_S. To make the comparison fair, we also consider a CUSUM version based on the Hotelling's T^2 statistic with the allowance constant chosen to be 0.1. This chart is denoted as GK_C. Both GK_S and GK_C do not consider surface registration. Their control limits are searched from the IC data such that their ARL_0 values equal the nominal ARL_0 value, as we did for $Q^+_{ART,i}$. The original GP method also provides a Shewhart chart using the Hotelling's T^2 statistic that is based on the difference between the predicted surface values of a Phase II surface at the so-called checkpoints and the mean predicted surface values at the same checkpoints obtained from a set of Phase I IC surfaces. Because the surface registration procedure discussed in Colosimo et al. (2014) cannot be used in the current setup, the one discussed in Section 2.1 is used here. In the Phase I IC dataset, we assume that there are 5,000 observed surfaces. The checkpoints are selected to be the 1,089 equally spaced grid points with both the $x-$ and $y-$coordinate values to be $\{-8, -7.5, \ldots, 0, \ldots, 7.5, 8\}$. This chart is denoted as $GP_{S,ART}$, where the subscript ART denotes the surface registration procedure discussed at the end of Section 2.1. To make the comparison fair, we also consider a CUSUM version with the allowance constant being 0.1, which is denoted as $GP_{C,ART}$. The control limits of $GP_{S,ART}$ and $GP_{C,ART}$ are searched from the IC data such that their ARL_0 values equal 20, as we did for

$Q^+_{ART,i}$. In the same setup as that in Table 2, the calculated ARL_1 values of GK_S, GK_C, $GP_{S,ART}$ and $GP_{C,ART}$ are presented in Table 5. In the table, some entry values are 200+ because we use 200 as the maximum number of observed surfaces in each simulation to calculate the run length of a control chart and the chart does not give any signal by the 200th time point. From the table, we can see that the GP method discussed in Colosimo et al. (2014) has a much better performance, compared to the method discussed in Wang et al. (2014), in the current example. We also notice that the ARL_1 values of GK_S and GK_C are even much larger than the nominal ARL_0 value in all cases considered. The bias can be explained by the lack of surface registration in these two charts, as we observed for the chart $Q^+_{A,i}$ in Tables 2 and 4, and by the fact that they impose several assumptions on the process distribution (cf., the related description in Section 1) which may not be valid here. By comparing the results in Tables 2 and 5, it can be seen that our proposed chart $Q^+_{ART,i}$ has a better performance than the charts considered here in all cases considered.

Table 5: Calculated ARL_1 values of the charts GK_S, GK_C, $GP_{S,ART}$ and $GP_{C,ART}$ in the setup of Table 2.

r_1	0	0.01	0.03	0.05	0.07	0.09	0.11	0.13	0.15	0.17	0.19	0.21
GK_S	19.97	54.59	106.83	200+	200+	200+	200+	200+	200+	200+	200+	200+
GK_C	19.82	53.56	184.39	200+	200+	200+	200+	200+	200+	200+	200+	200+
$GP_{S,ART}$	20.46	19.81	19.66	16.95	17.22	16.06	13.94	12.18	11.78	10.52	9.26	8.50
$GP_{C,ART}$	20.31	20.63	19.38	17.47	16.58	14.18	13.12	12.26	10.78	10.77	9.19	8.80

In all above examples, the value of ARL_0 is set to be 20, which is relatively small, compared to the commonly used ARL_0 values in the literature. This small value is used here because the number of the same kind of products produced by a 3D printer is usually small. Next, we consider an example in the same setup as that in Table 2, except that ARL_0 is chosen to be 200. The calculated ARL_1 values of the charts $Q^+_{SRT,i}$, $Q^+_{ART,i}$, $Q^+_{AT,i}$, and $Q^+_{A,i}$ are shown in Table 6. From the table, it can be seen that similar conclusions to those from Table 2 can be made here. More specifically, the chart $Q^+_{ART,i}$ performs the best for detecting relatively small shifts, the chart $Q^+_{SRT,i}$ is the best for detecting relatively large shifts, and the charts $Q^+_{AT,i}$ and $Q^+_{A,i}$ do not perform well in all cases considered.

Table 6: ARL_1 values of the Phase II CUSUM charts when $ARL_0 = 200$, $k = 0.1$ or 0.5, the OC surface is $g^{(1)}(x, y)$, and the shift parameter r_1 takes various different values. Numbers in parentheses are standard errors.

r_1	$Q^+_{SRT,i}$		$Q^+_{ART,i}$		$Q^+_{AT,i}$		$Q^+_{A,i}$	
	$k = 0.1$	$k = 0.5$	$k = 0.1$	$k = 0.5$	$k = 0.1$	$k = 0.5$	$k = 0.1$	$k = 0.5$
0	200.89(4.14)	200.45(4.37)	199.33(3.89)	199.01(4.02)	199.38(4.15)	199.28(4.19)	200.05(4.18)	201.023(4.31)
0.01	157.10(3.29)	165.05(3.40)	145.08(2.90)	167.87(3.50)	176.46(3.52)	172.82(3.71)	183.18(3.52)	193.45(6.11)
0.03	48.87(0.20)	95.54(1.80)	34.67(0.53)	70.28(1.57)	131.74(2.66)	117.34(2.56)	164.01(3.35)	177.64(5.62)
0.05	15.47(0.15)	20.98(0.34)	12.93(0.10)	15.55(0.24)	84.96(1.59)	92.34(2.00)	142.86(2.85)	150.20(4.75)
0.07	7.20(0.04)	6.99(0.06)	7.08(0.04)	5.90(0.05)	61.22(1.09)	57.14(1.17)	132.02(2.58)	134.31(4.25)
0.09	4.43(0.02)	3.48(0.02)	4.66(0.02)	3.57(0.02)	41.61(0.68)	42.81(0.88)	118.45(2.25)	128.22(4.05)
0.11	3.09(0.01)	2.24(0.01)	3.59(0.01)	2.48(0.01)	32.80(0.48)	30.51(0.59)	102.45(1.91)	113.00(3.57)
0.13	2.26(0.01)	1.77(0.01)	2.84(0.01)	2.00(0.01)	25.43(0.33)	22.49(0.43)	98.67(1.98)	100.40(3.17)
0.15	1.97(0.01)	1.17(0.01)	2.33(0.01)	1.79(0.01)	20.83(0.27)	17.67(0.32)	81.54(1.52)	93.75(2.96)
0.17	1.73(0.01)	1.00(0.00)	2.01(0.00)	1.39(0.01)	17.36(0.20)	14.00(0.25)	77.89(1.46)	78.15(2.47)
0.19	1.02(0.00)	1.00(0.00)	1.97(0.00)	1.07(0.01)	14.41(0.14)	11.42(0.19)	64.68(1.17)	74.38(2.35)
0.21	1.00(0.00)	1.00(0.00)	1.96(0.00)	1.00(0.00)	12.63(0.12)	9.61(0.16)	62.53(1.12)	66.45(2.11)

4 A Real-Data Example

In this section, we illustrate the proposed Phase II surface monitoring CUSUM chart (9)-(10) using a real 3D printer and its products. The 3D printer and the laser scanner used here are the ones shown in Figure 1, owned by the Marston Science Library of the University of Florida. The IC product looks like the one shown in the upper-right panel of Figure 1, with the design space to be $[-30, 30] \times [-30, 30]$ (in mm^2) and the z values (i.e., heights at different (x, y) positions) in the range $[10, 30]$ mm. The top surface of the designed IC product is shown in the bottom-right panel of Figure 1. For each product, the number of observations in each observed surface generated by the laser scanner ranges between 141,000 and 158,500.

The 3D printer then prints 15 products under our careful operation and the observed surfaces of these 15 products are used as the IC data. We then use the IC data to set up the four related control charts $Q^+_{SRT,i}$, $Q^+_{ART,i}$, $Q^+_{AT,i}$ and $Q^+_{A,i}$. In all charts, we choose $k = 0.5$ and $ARL_0 = 20$. The control limits of the charts are determined by the bootstrap procedure with the bootstrap sample size $B = 10,000$, as discussed at the end of Section 2. The calculated control limits of the charts $Q^+_{SRT,i}$, $Q^+_{ART,i}$, $Q^+_{AT,i}$ and $Q^+_{A,i}$ are 2.19, 1.83, 1.58 and 1.79, respectively.

Next, we let the 3D printer print 4 IC products and 5 OC products as the Phase II data. The 5 OC products have shifts with different shapes and sizes. All 9 Phase II products are ordered in the way that the four IC products are placed at the first 4 positions and the 5 OC products are placed afterwards with their shift sizes increasing over time. The observed top surfaces of the 5 OC products are shown in Figure 3, along with the top surface of an IC product. All these surfaces are the original ones without surface registration.

We then use the four CUSUM charts $Q^+_{SRT,i}$, $Q^+_{ART,i}$, $Q^+_{AT,i}$ and $Q^+_{A,i}$ for monitoring the 9 Phase II products. The four control charts are shown in Figure 4. From the plots in that figure, it can be seen that (i) both the charts $Q^+_{SRT,i}$ and $Q^+_{ART,i}$ can detect the process shift at the 5th time point well, and (ii) the charts $Q^+_{AT,i}$ and $Q^+_{A,i}$ both give signals too early because they did not register the observed surfaces properly in advance and surface registration is important in the 3D printing application, as discussed in Section 1.

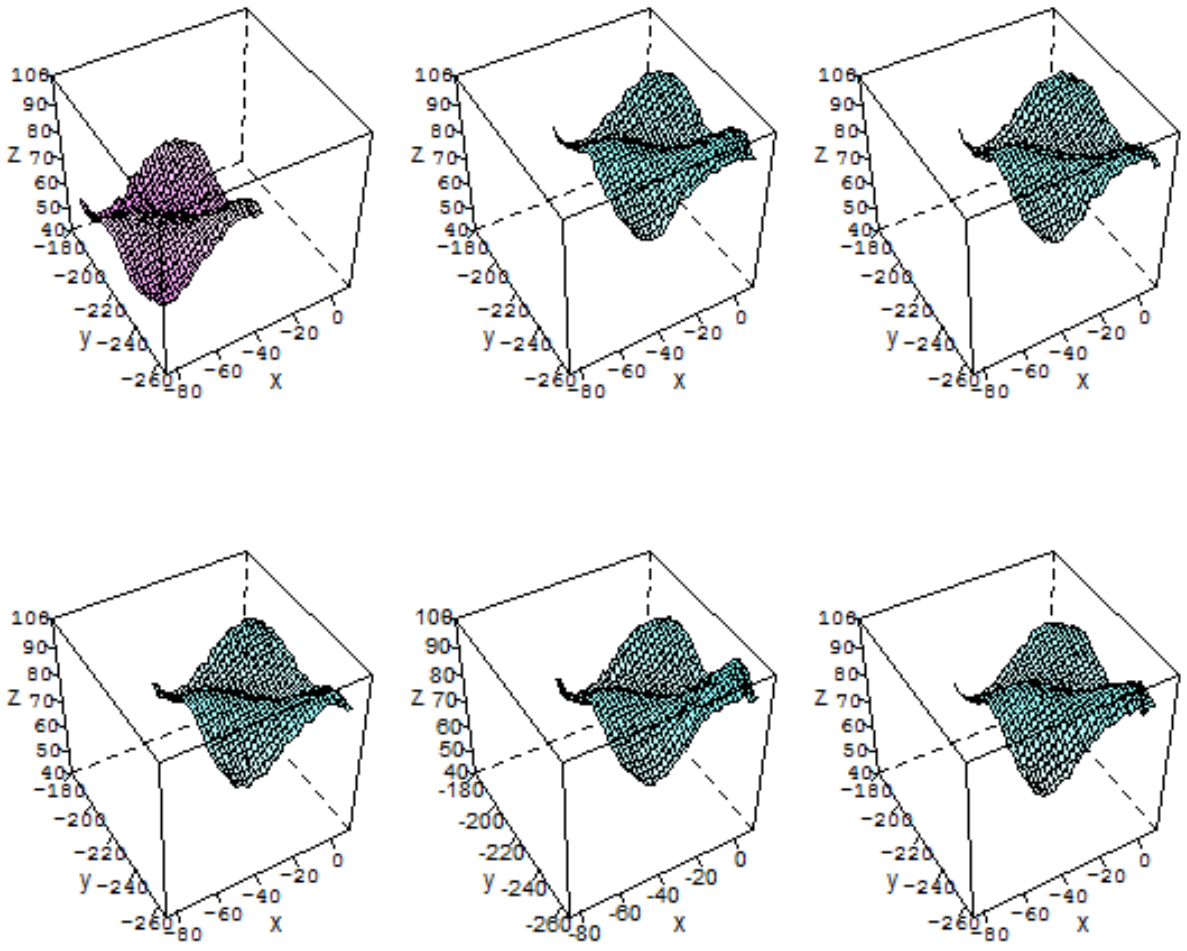

Figure 3: The first surface is from an IC product, and the remaining surfaces are from 5 OC products.

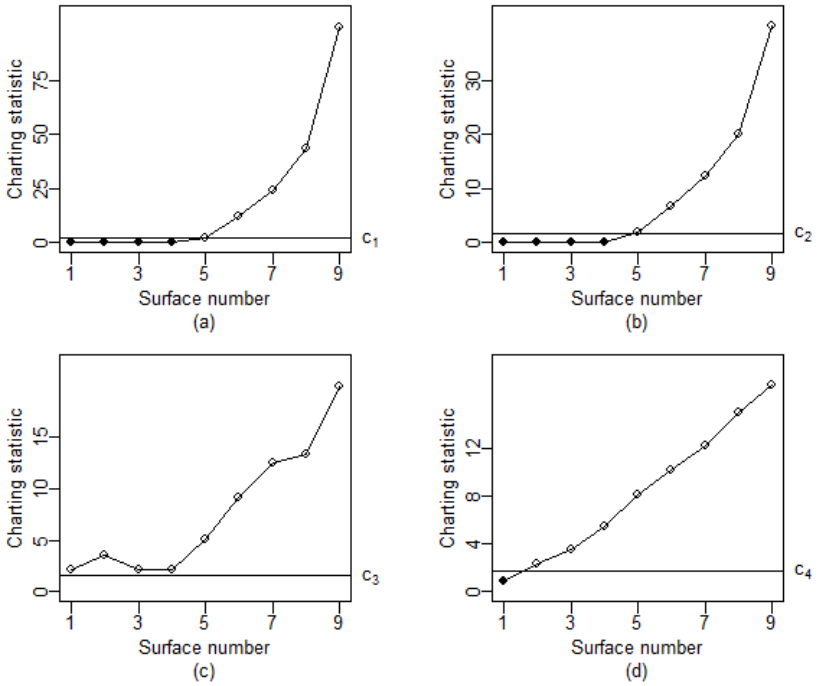

Figure 4: Phase II CUSUM charts for monitoring 3D printing products. (a) $Q^+_{SRT,i}$, (b) $Q^+_{ART,i}$, (c) $Q^+_{AT,i}$, and (d) $Q^+_{A,i}$.

5 Conclusion and Future Work

In the previous sections, we have described our proposed CUSUM charts for Phase II online monitoring of the free-form surfaces of 3D printing products. Numerical examples show that the proposed method performs reasonably well in practice. However, the current method still has some limitations. For instance, in models (3) and (7), the random noise is assumed i.i.d.. In reality, spatial and temporal correlation might exist. If the spatial-temporal correlation is the same in the IC data and Phase II data, then our proposed method should still be valid, because its control limit is determined from the IC data by a bootstrap procedure, although a block bootstrap procedure might be more appropriate to use in such cases and its efficiency might be improved if the spatial-temporal correlation can be used in the construction of the control chart. Also, in the current method, only the top surface of a 3D printing product is monitored. In certain applications, we might want to monitor the surface of the entire 3D product, which is not discussed in the paper. From the real-data example in Section 4, we can see that an observed surface in 3D printing usually contains a large number of observations. Therefore, surface registration and surface estimation in the proposed method involve extensive computation. More computing efficient methods are definitely

needed. All these issues will be addressed carefully in our future research.

Acknowledgments: The authors thank the guest co-editors and two referees for many constructive comments and suggestions which improved the quality of the paper greatly. This research was supported in part by an NSF grant.

References

Audette, M. A., Ferrie, F. P., and Peters, T. M. (2000). An algorithmic overview of surface registration techniques for medical imaging. *Medical image analysis*, **4**, 201-217.

Bhagalia, R., Fessler, J., and Kim, B. (2009). Accelerated nonrigid intensity-based image registration using importance sampling. *IEEE Transactions on Medical Imaging*, **28**, 1208-1216.

Colosimo, B. M., Cicorella, P., Pacella, M., and Blaco, M. (2014). From profile to surface monitoring: Spc for cylindrical surfaces via Gaussian processes. *Journal of Quality Technology*, **46**, 95-113.

Denton, E., Sonoda, L., Rueckert, D., Rankin, S., Hayes, C., Leach, M., Hill, D., and Hawkes, D. (1999). Comparison and evaluation of rigid, affine, and nonrigid registration of breast mr images. *Journal of Computer Assisted Tomography*, **23**, 800-805.

Evans B. (2012). *Practical 3D Printers: The Science and Art of 3D Printing.* Apress Publisher.

Jin, J. and Shi, J. (1999). Feature-preserving data compression of stamping tonnage information using wavelets. *Technometrics*, **41**, 327-339.

Kang, L. and Albin, S. (2000). On-line monitoring when the process yields a linear profile. *Journal of Quality Technology*, **32**, 418-426.

Kim, K., Mahmoud, M., and Woodall, W. (2003). On the monitoring of linear profiles. *Journal of Quality Technology*, **35**, 317-328.

Pan, W., Qin, K., and Chen, Y. (2009). An adaptable-multilayer fractional fourier transform approach for image registration. *IEEE Transactions on Pattern Analysis and Machine Intelligence*, **31**, 400-412.

Paynabar, K., Jin, J., and Pacella, M. (2013), "Analysis of multichannel nonlinear profiles using uncorrelated multilinear principal component analysis with applications in fault detection and diagnosis," *IIE Transactions*, **45**, 1235-1247.

Paynabar, K., Qiu, P., and Zou, C. (2016), "A change point approach for Phase-I analysis in multivariate profiles monitoring and diagnosis," *Technometrics*, **58**, 191-204.

Qiu, P. (2005). *Image Processing and Jump Regression Analysis*. New York: John Wiley & Sons.

Qiu, P. (2014). *Introduction to Statistical Process Control*. Boca Raton, FL: Chapman Hall/CRC.

Qiu, P. and Xing, C. (2013). On nonparametric image registration. *Technometrics*, **55**, 174-188.

Qiu, P., Zou, C., and Wang, Z. (2010). Nonparametric profile monitoring by mixed effects modeling (with discussions). *Technometrics*, **52**, 265-293.

Wang, A., Wang, K., and Tsung, F. (2014), "Statistical surface monitoring by spatial-structure modeling," *Journal of Quality Technology*, **46**, 359-376.

Xia, H., Ding, Y., and Wang, J. (2008). Gaussian process method for form error assessment using coordinate measurements. *IIE Transactions*, **40**, 931-946.

Xing, C. and Qiu, P. (2011). Intensity based image registration by nonparametric local smoothing. *IEEE Transactions on Pattern Analysis and Machine Intelligence*, **33**, 2081-2092.

Yeh, A. B., Huwang, L., and Li, Y.-M. (2009). Profile monitoring for a binary response. *IIE Transactions*, **41**, 931-941.

Zang and Qiu (2017). Phase I monitoring of spatial surface data from 3D printing. *Technometrics*, in press.

Zou, C., Tsung, F., and Wang, Z. (2008). Monitoring profiles based on nonparametric regression methods. *Technometrics*, **50**, 512-526.